

deepCR: Cosmic Ray Rejection with Deep Learning

KEMING ZHANG (张可名)¹ AND JOSHUA S. BLOOM^{1,2}

¹*Department of Astronomy, University of California, Berkeley, CA 94720-3411, USA*

²*Lawrence Berkeley National Laboratory, 1 Cyclotron Road, MS 50B-4206, Berkeley, CA 94720, USA*

(Received –; Revised –; Accepted –)

Submitted to ApJ

ABSTRACT

Cosmic ray (CR) identification and removal are critical components of imaging and spectroscopic reduction pipelines involving solid-state detectors. We present **deepCR**, a deep learning based framework for cosmic ray (CR) identification and subsequent image inpainting based on the predicted CR mask. To demonstrate the effectiveness of our framework, we have trained and evaluated models on Hubble Space Telescope ACS/WFC images of sparse extragalactic fields, globular clusters, and resolved galaxies. We demonstrate that at a reasonable false positive rate of 0.5%, **deepCR** achieves close to 100% detection rates in both extragalactic and globular cluster fields, and 91% in resolved galaxy fields, which is a significant improvement over current state-of-the-art method, **LACosmic**. Compared to a well-threaded CPU implementation of **LACosmic**, **deepCR** mask predictions runs up to 6.5 times faster on CPU and 90 times faster on GPU. For image inpainting, mean squared error of **deepDR** predictions are 20 times lower in globular cluster fields, 5 times lower in resolved galaxy fields, and 2.5 times lower in extragalactic fields, compared to the best performing non-neural technique. We present our framework and trained models as an open-source **Python** project, with a simple-to-use API.

Keywords: instrumentation: detectors - methods: data analysis - techniques: image processing

1. INTRODUCTION

Charged particles passing through solid state detectors, such as charged coupled devices (CCDs), can corrupt astronomical imaging and spectroscopy by creating electron-hole pairs which in turn causes excess flux in the pixels hit. Colloquially called “cosmic rays” (CRs), such charge particles can be terrestrial, instrumental, and cosmic in origin. The majority of CRs which affect CCDs in ground-based observatories are secondary muons from high-energy showers, though radioactivity from instrument optics and dewar materials also contribute (Groom 2004; Florentin-Nielsen et al. 1995). Images taken with space-based facilities, such as the Hubble Space telescope (HST), are more prone to cosmic ray contamination, with the main culprit being electrons and protons trapped in Earth’s radiation belt, that originated in the solar wind.

Cosmic ray artifacts must be identified and either masked or replaced, before further analysis could be done on the image. It is straightforward to identify these artifacts when multiple exposures of the same field are taken. In such cases, a median image could be calculated from aligned single exposures, effectively creating a CR-free image. Each one of the exposures is then compared with the median image to identify the cosmic rays (cf. Windhorst et al. 1994).

However, when CCD read-out times are non-negligible, or when sources of interest are transient or variable, cosmic ray rejection with multiple exposures can be sub-optimal. These cases would require methods that find CRs in single exposures, such as linear filtering (Rhoads 2000), median filtering (IRAF **xzap**), Laplacian edge detection (van Dokkum 2001; **LACosmic**), histogram analysis (Pych 2004), among others. Farage & Pimblet (2005) evaluated the aforementioned methods and found **LACosmic** to be the most effective. **LACosmic** identifies CRs by performing Laplacian transformations on upsampled input images to find CR edges, which

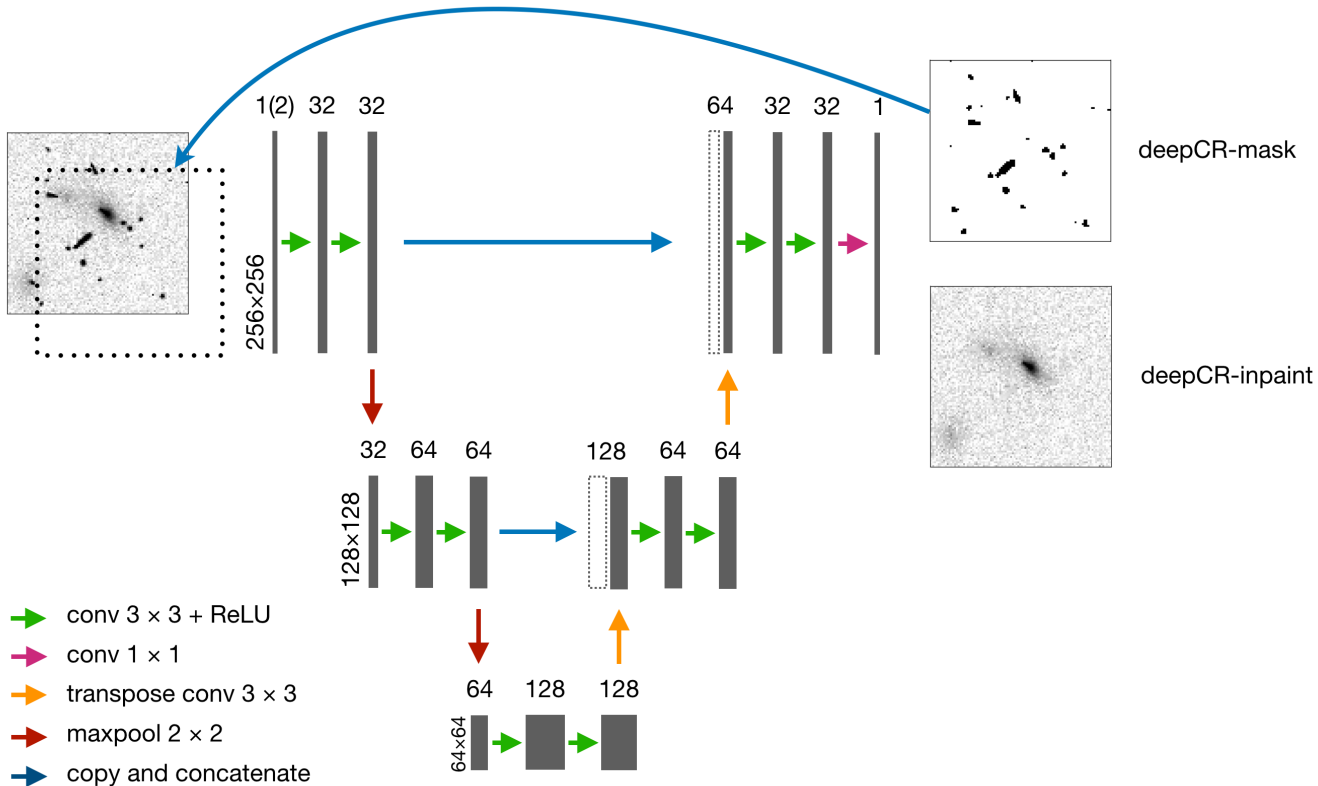


Figure 1. Neural network architecture of **deepCR**. Feature maps are represented by gray boxes while the number of channels and example feature map dimensions are indicated on the top of and to the left of each feature map, respectively. Different computational operations are marked in the legend to the lower left. Unfilled boxes to the right of blue arrows represent feature maps directly copied from the left, which are to be concatenated with the adjacent feature map. To apply the inpainting model, the predicted mask (dotted box at left) is concatenated with the original image as the input.

tend to be much sharper than those of astronomical objects because cosmic ray artifacts are not smeared out by the atmosphere or telescope optics. Since edges only lie on the CR boundary, **LACosmic** must be run iteratively to mask larger CRs, with each successive step progressively identifying and replacing CR artifacts from the outermost pixels. Additionally, while Laplacian edge detection is very effective on well-sampled images, it can include many false detections when the point spread function (PSF) is critically sampled, as in the case of HST images. **LACosmic** tackles this by adding an additional symmetry criteria, which distinguishes arbitrarily shaped CRs from symmetrical PSF spread-out point sources.

In addition to the methods mentioned above, machine learning (ML) techniques for which classification rules are learned from labeled training data, have also been previously applied to CR detection; this includes neural networks (Murtagh & Adorf 1991), k-nearest neighbors, and decision trees (Salzberg et al. 1995). However, these techniques have generally under-performed **LACosmic**. In this paper, we present a deep learning

based method for cosmic ray identification and replacement, which leverages recent progress in deep learning and computer vision. Central to these two fields are convolutional neural networks (CNNs; cf. LeCun et al. (2015)) which, in contrast to kernel convolution in **LACosmic**, allow for kernels to be learned through back-propagation instead of being user-specified. In addition, compared with single-layer convolution, CNNs convolve feature maps recursively to potentially large depths, thus allowing semantic features to be extracted, in addition to low-level pixel features such as the location of edges. Recent developments in CNN architecture have advanced not only image classification (Deng et al. 2009), but also image segmentation (e.g., Shelhamer et al. (2017)), which refers to the process of labeling each pixel as belonging to a set of categories, and image inpainting, which refers to the process of predicting the missing or corrupted part of an image (Lehtinen et al. 2018). In the context of CR rejection, image segmentation is a binary classification between cosmic ray artifact and non-artifact, while replacing pixel values under CR masks is essentially image inpainting.

Our primary interest in this paper is to develop a deep learning based CR detection and replacement method that is both more robust than existing techniques, and at least as fast to run. We motivate and define the architecture of our model in Section 2, after which we discuss dataset construction in Section 3. In Section 4, we benchmark the performance of our model against baseline methods. A discussion of the results can be found in Section 5. Our framework and trained models are offered as an open-source project in Python with a simple-to-use API.¹

2. MODEL ARCHITECTURE

We formulate our framework as a sequence of two independent deep neural networks, `deepCR-mask` and `deepCR-inpaint`, for which `deepCR-mask`, given an input image, predicts a probabilistic map of each pixel being affected by cosmic rays, and `deepCR-inpaint` predicts what the pixels values would have been had they not been affected by cosmic rays. The probability map predicted by `deepCR-mask` is then turned into a binary cosmic ray mask, i.e., 1 denoting cosmic ray, and 0 denoting non-artifact, by setting a threshold. The input image is then concatenated with the binary mask to be fed into `deepCR-inpaint`, which outputs an image with the pixel values under the inpaint mask as the predicted values. The masked pixel values in the input image are set to 0 before feeding into concatenation. `deepCR-mask` and `deepCR-inpaint` are independently trained and can be used separately at application time. This means that `deepCR-inpaint` could take in any mask for inpainting so long as the unmasked pixels are free from cosmic ray artifacts.

The basic architecture of both `deepCR-mask` and `deepCR-inpaint` is the UNet (Ronneberger et al. 2015), which is an encoder-decoder CNN with residual connections between each depth of the encoder and decoder (Figure 1). UNet was first formulated for biomedical image segmentation and further adapted to a wide range of segmentation tasks. Since UNet is fully convolutional and convolutional layers are translation invariant, it is not restricted to input images of fixed-dimension.

The encoder extracts lower level pixel features such as edges at the first convolution layers, while deeper layers in the encoder closer to the network bottleneck generate higher level semantic information, e.g., location and properties of cosmic rays and stars. Information passes from the encoder to the decoder via the bottleneck and residual connections. The decoder up-samples the encoded information back to an output image in

the original resolution. The residual connections allow the decoder to have direct access to low level image feature, and thus are important components of the network because they allow the decoder to know not only the approximate location of cosmic ray artifacts (high-level features), but also their exact boundaries (low-level features).

Training `deepCR-mask` and `deepCR-inpaint` requires a set of training data which consists of cosmic ray affected input images (X) and ground truth cosmic ray masks (M). Our training data is constructed from Hubble Space Telescope images and includes multiple exposures of the same fields that provides the basis for us to derive accurate ground truth cosmic ray masks by comparing each exposure with a median image. Construction of the dataset is discussed in Section 3.

We use the binary cross-entropy loss in training `deepCR-mask`,

$$\mathcal{L}_F = \mathbb{E}[M \times \log(1 - F(X)) + (1 - M) \times \log(F(X))], \quad (1)$$

where F refers to `deepCR-mask` and expectation is with respect to training data. This loss essentially penalizes the log probability of each pixel prediction being wrong. For `deepCR-inpaint`, mean square error (MSE) loss is taken between the predicted pixels under the inpainting mask (M_I) and the ground truth values. While at first glance this would require having ground truth pixel values of CR artifact pixels, which are available to use in the median image, such necessity is easily circumvented by generating alternative inpainting masks in regions of the image that are not contaminated by cosmic rays. In practice, we select and add up one or more CR masks of other image stamps in the dataset as the inpainting mask; this naturally allows for data augmentation (see Section 3.1). One difference between using the median image as ground truth and the input image itself is that the median image is less noisy. Although at first glance training on higher S/N targets could be advantageous, Lehtinen et al. (2018) showed that training on noisy targets is comparable to training on clean targets in terms of convergence speed and final performance. The inpainting loss is then formulated as,

$$\mathcal{L}_G = \mathbb{E}[(G(X, M_I) \circ M_I \circ (1 - M) - X \circ M_I \circ (1 - M))^2], \quad (2)$$

where \circ denotes element-wise multiplication. Here, G refers to `deepCR-inpaint`, X the input image, M the cosmic ray mask, and M_I the inpaint mask. Element-wise multiplication by $(1 - M)$ ensures loss not be taken for parts of the inpaint mask overlapping with cosmic ray hits in the image. Loss is also not taken outside of

¹ <https://github.com/profjsb/deepCR>

Table 1. Hubble ACS/WFC F606W fields used in dataset construction. Test data is marked with an asterisk (*).

Proposal ID	Visit Num.	Type	N_{exp}	t_{ave} [sec]
10420	01	extragalactic field	3	660
10420	05	extragalactic field	3	660
10420	07	extragalactic field	3	660
12213	11	extragalactic field	6	418
13671*	44	extragalactic field	3	400
10775*	06	globular cluster	4	100
10775	07	globular cluster	4	140
10775	08	globular cluster	5	380
10775*	09	globular cluster	5	350
10260	03	resolved galaxy	3	790
10260	04	resolved galaxy	3	790
10260	06	resolved galaxy	3	790
10260	08	resolved galaxy	3	790
10584	32	resolved galaxy	3	527
10190*	28	resolved galaxy	4	540

the inpaint mask; otherwise `deepCR-inpaint` is forced to also learn an identity function for those regions, which is both unnecessary and degrades model performance given fixed model capacity.

In our experiments, we also considered using a mean absolute error loss (L1) weighted by the inverse of image noise (Poisson and read noise). Although this loss is statistically better grounded, it penalizes predictions of sky background pixel much more than pixels with actual astrophysical flux. Considering that background pixels are already heavily weighted by the sheer number, and that pixel values of stars and galaxies are much harder to predict, we opt for the well-behaving MSE error instead.

3. DATA

We have constructed our training and testing datasets from Hubble Space Telescope ACS/WFC imaging data, using the `ASTRODRIZZLE` (Hack et al. 2012) data pipeline. The imaging data we used is listed in Table. 2, and is divided into three categories: extragalactic field, globular cluster, and local group galaxies for which the stellar population is well resolved; the density of astronomical sources, which are also sources of confusion during CR identification, increases in that order. While we train simultaneously on the three categories of data, evaluation is done separately to examine the performance of each model on tasks of various difficulty.

Each set of image consists of 3 to 6 single exposures. `ASTRODRIZZLE` creates a cosmic ray free image for each calibrated single frame exposure (`*flc.fits`) by align-

ing every frame to sub-grid accuracy and calculating a median image, before “blotting” the median image into the grid of each individual exposure. It then identifies cosmic rays in each frame by comparing with both the median image and the derivative median image which accounts for discrepancies caused by alignment residuals. Cosmic ray is then identified from the difference image with two passes. A cosmic ray mask is first produced with a high S/N threshold to minimize false detections. Pixels adjacent to the ones found in the first pass, specified by a growing radius (set to 1), is examined with a lower S/N threshold to identify the dimmer peripherals of each cosmic ray. While the default S/N threshold is 3.5 and 3 for the first and second pass, we opted for 5 and 1.5 because the default first threshold causes many false positives and the second threshold is not low enough for it to identify dimmer peripherals.

To ensure good training behavior, we also created a bad pixel mask and a saturation mask for which we do not backpropagate through nor evaluate the models on. The bad pixel masks are derived from the data quality array in the `*flc.fits` files where we include all flags except the saturation flag. We create a conservative saturation mask by masking pixels brighter than $70000 e^-$, which we further expand with a radius-7 square dilation kernel to make sure that the peripherals of blooming artifacts are covered.

Finally, we divide the images and masks into image stamps of 256×256 to facilitate batch training. Because each single frame image may be slightly offset from each other for our dataset, we discard the first 128 pixels at the image boundary and keep only the central region with overlap of at least one other exposure. Each frame of exposure then yields 210 image stamps. This results in a training set of 8190 image stamps and a test set of 3360 image stamps. We further reserve 1638 image stamps from the training set as the validation set to monitor over-fitting during training. To prevent hiding over-fitting during evaluation, test set images are chosen to have different target fields than the training images and a wide range of exposure times.

3.1. Data Augmentation

During both training and evaluation, we create an inpainting mask for each image by sampling and adding 1-9 cosmic ray masks from the rest of the training set. Our augmentation scheme allows the `deepCR-inpaint` to adapt to inpaint masks of various density (Figure. 3); having denser inpainting masks also allows more efficient training.

Additionally, we also augment sky background level for the input images in training both `deepCR-mask` and

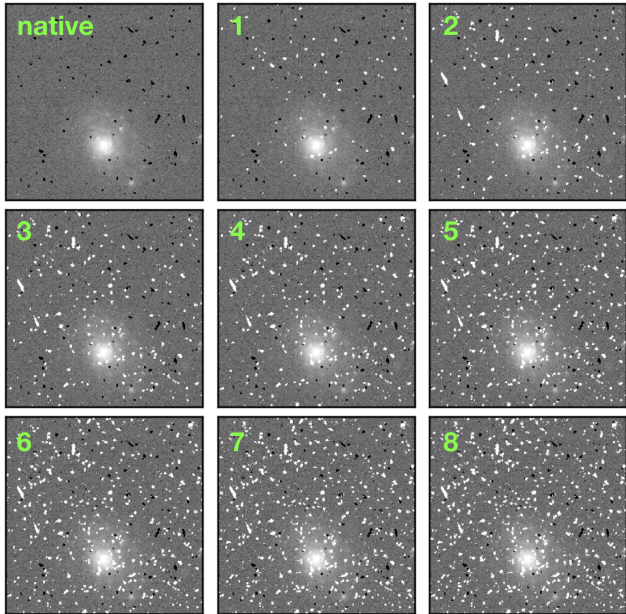


Figure 2. Data augmentation scheme of creating inpaint masks. Numbers indicate the number of CR masks sampled and stacked from the dataset to create the inpaint mask, as shown in white. The original CR artifacts are masked in black to distinguish them from the inpainting mask.

deepCR-inpaint, to remedy for the limited and discrete exposure times in the training set. Different exposure times and sky background levels mainly change the contrast of cosmic ray artifacts (as well as astronomical objects) against the background, which can affect model prediction. We adjust the sky background level by adding up to 3 times and subtracting up to 0.9 times the original level. Since the pixel value can be written as

$$n = (f_{\text{star}} + f_{\text{sky}}) \cdot t_{\text{exp}} + n_{\text{CR}}, \quad (3)$$

where n is in units of e^- and flux (f) in units of e^-/s , pixel value after augmentation would be

$$n' = n + \alpha \cdot f_{\text{sky}} \cdot t_{\text{exp}} = \left(\frac{f_{\text{star}}}{1 + \alpha} + f_{\text{sky}} \right) \cdot (1 + \alpha) \cdot t_{\text{exp}} + n_{\text{CR}}. \quad (4)$$

Thus, adding or subtracting a multiplicative of sky level, i.e., $\alpha \cdot f_{\text{sky}}$, is equivalent to simulating an exposure time of $(1 + \alpha) \cdot t_{\text{exp}}$, with flux from astronomical objects scaled down by $1 + \alpha$, which is of minimal concern since astronomical fluxes already span orders of magnitude. Although alternatively one may simulate different exposure times by directly scaling the image with a multiplicative factor, doing so would lead to different cosmic ray statistics, whose contribution to pixel value is independent of time. We do note that such an augmentation scheme would inevitably change image noise properties in the image and therefore only approximate different

exposure times; however, following similar arguments in Lehtinen et al. (2018), homogeneous noise should have little effect on training. In our experiments, we observed that model trained with sky background augmentation performed significantly better on test data augmented in the same way, and equally well on native test data. On real data, deepCR-mask trained with augmentation improves detection rates for the shortest exposure (100s) test image set (HST 10775-06) by $\sim 2\%$ when images with exposure times less than 400s are withheld from the training set. Including these short exposure data in our training set did not further improve our metrics. This shows that the sky background augmentation scheme is as helpful as having more data of different exposures. We therefore omitted short exposure globular cluster data from deepCR-mask training set.

4. RESULTS

We label each variant of our network with two hyper-parameters, i.e., deepCR-3-32 would be a depth-3 network with 32 channels at the convolution layer (same as Figure 1). The labels of mask and inpaint are omitted whenever context is evident. For deepCR-mask, we trained two different variants: deepCR-2-4 and deepCR-2-32. We also tried architectures as large as deepCR-4-64, but did not see significant improvements from deepCR-2-32. For deepCR-inpaint, we trained and evaluated on deepCR-2-32 and deepCR-3-32. Details on training can be found in Appendix A. We benchmarked network performances against baseline models, and describe the results as follows.

4.1. Cosmic Ray Identification: deepCR-mask

We evaluate deepCR-mask with Receiver Operating Characteristic curves (ROC curves), against the baseline model of LACosmic. ROC curves show true positive rates (fraction of cosmic ray artifact pixel identified) as a function of false positive rates (fraction of pixels mistaken as cosmic ray) and are plotted by dialing the threshold parameter of a given model. For LACosmic, an additional parameter `objlim` that controls the symmetry discriminant (the "fine structure image") needs to be tuned for its optimal performance. We have experimented with a range of values, and found `objlim`=2, 3.5, and 5 to be the optimal values for images of extragalactic fields, globular cluster, and resolved galaxy, respectively. We note that `objlim`=2 and 3.5 are smaller than the recommended value of 4 - 5 for HST WFPC in the original LACosmic documentation, but smaller `objlim` value allows fewer cosmic ray to be discounted on the basis of symmetry, which is advantageous when few unresolved sources of confusion are present in the image.

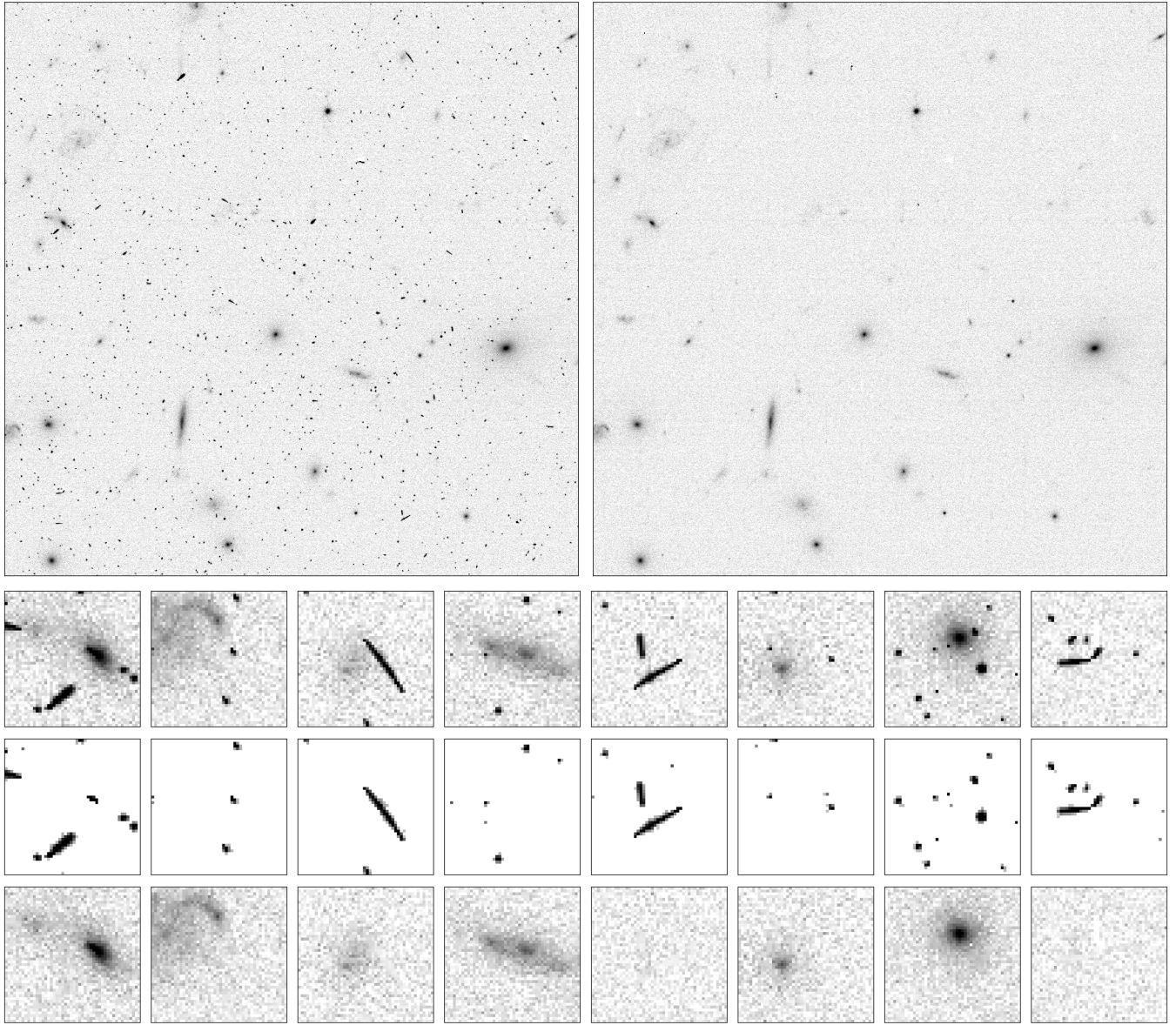


Figure 3. (left) ACS/WFC image of galaxy cluster EMACSJ2316.6 (HST:13671-44). (right) same image with cosmic ray removed and inpainted by `deepCR`. (bottom) Top row shows details of cosmic ray artifacts. Middle panel shows cosmic ray as identified by `deepCR-mask-2-32`. Bottom panel shows the image with artifact pixels replaced by `deepCR-inpaint-3-32`.

Figure 3.1 shows ROC curves of `deepCR-2-32` (hereafter `deepCR`) and `LACosmic` evaluated on the three categories of data in the test set. As seen in the black curves in figure 3.1, at fixed false positive rates (FPR), `deepCR` was able to achieve much higher true positive rates (TPR) compared with `LACosmic` for all three fields. While `deepCR` was able to achieve nearly 100% TPRs for both extragalactic fields and globular cluster fields and $\geq 90\%$ for resolved galaxy fields, the detection rates of `LACosmic` is constantly below 80% for the same FPR range.

However, to make a conclusion from here would be unfair to `LACosmic`. The main reason is that imaging noise

makes it impossible to create objective ground truth cosmic ray masks, and the characteristic way by which `drizzlepac` create cosmic ray masks could be learned by `deepCR` during training but not `LACosmic`. In particular, we adapted relatively liberal thresholds in the two-step cosmic ray identification procedure in `drizzlepac` to minimize residual cosmic ray flux in the image, but `LACosmic` is more conservative and sometimes ignores the peripheral pixels of larger cosmic rays. In practice, users may choose to expand the predicted mask for a more conservative treatment of cosmic rays. Therefore, to remove any aforementioned advantage `deepCR` may have gained, we re-calculated true positive rates

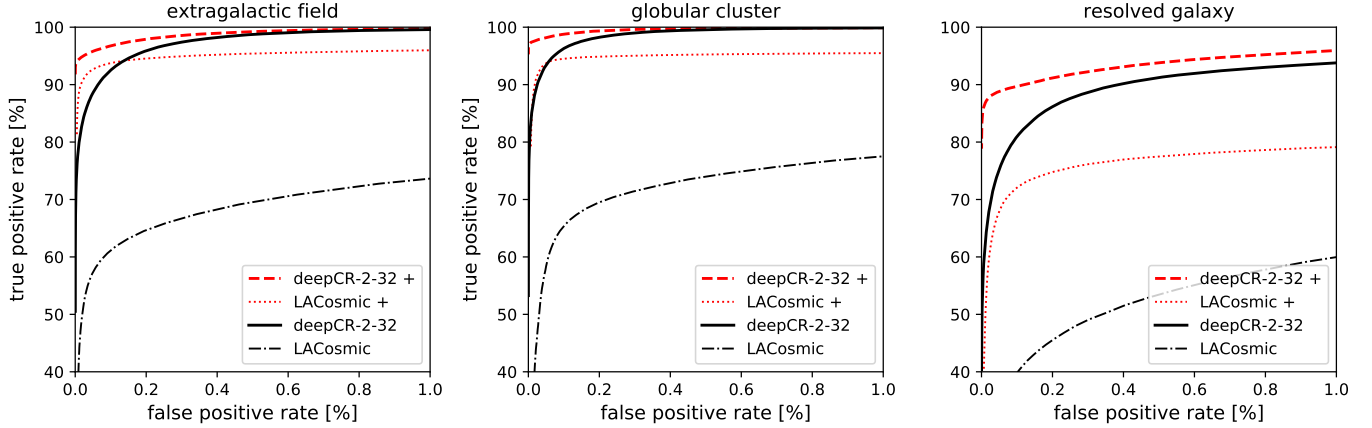


Figure 4. Receiver operating characteristic (ROC) curves of cosmic ray detection. Line shapes and the corresponding method are indicated in the legends to the lower right. Different points on the ROC curves correspond to different threshold parameters adapted in `deepCR` and `LACosmic`. Red ROC curves (labeled with + in the legend) differ from black ones in that true positive rates are calculated from a 3-square kernel dilated predicted mask, with false positive rates kept the same at the non-dilated values. The red curves therefore does not penalize a model for not finding the exact cosmic ray shape matching the ground truth.

Table 2. Cosmic ray true detection rates (TPR) evaluated on images of extragalactic field, globular cluster, and resolved galaxy, at fixed false positive rates (FPR) of 0.05% and 0.5%, shown in top and bottom tables respectively. Fixed FPRs are specified in the headers. TPRs in parenthesis show detection rates after mask dilation, as described in the main text. The last two columns show runtime required to predict CR masks for one hundred 256×256 images, evaluated on either 4 cores of an Intel Xeon CPU, or 1 Nvidia Titan X GPU.

Model	extragalactic field	globular cluster	resolved galaxy	runtime	
	TPR (0.05%)	TPR (0.05%)	TPR (0.05%)	CPU	GPU
deepCR-2-4	82.0% (94.5%)	83.9% (97.3%)	56.2% (80.4%)	1.4s	0.1s
deepCR-2-32	88.5% (95.8%)	93.3% (98.1%)	75.2% (88.8%)	7.9s	0.2s
LACosmic	57.3% (92.6%)	58.3% (93.7%)	33.8% (67.9%)	9.0s	n/a
<hr/>					
	TPR (0.5%)	TPR (0.5%)	TPR (0.5%)		
deepCR-2-4	94.0% (96.9%)	96.2% (98.7%)	80.6% (89.7%)		
deepCR-2-32	98.7% (99.2%)	99.5% (99.7%)	91.2% (93.7%)		
LACosmic	69.5% (95.4%)	73.9% (95.2%)	53.4% (77.4%)		

for both models using a radius-3 square kernel dilated (expanded) output mask, while keeping FPRs fixed at values evaluated on non-dilated masks. Radius-3 square dilation essentially masks all 9 pixels in any 3×3 region as long as the center pixel is identified as cosmic ray in the original mask. The re-calculated ROC curves, shown in red in Fig. 3.1, therefore does not penalize a model for not finding the exact cosmic ray shape matching the ground truth, thereby removing any advantage `deepCR` may have gained.

As expected, mask dilation increased true detection rate drastically for `LACosmic`, and also slightly improving ours at the very low-end of FPRs. However, our model still leads a significant edge in all three types of fields. `LACosmic` detection rates in extragalactic fields

and globular cluster fields are increased to up to 95% where the ROC curve plateaus; 5% of CRs are consistently missed regardless of detection threshold. In resolved galaxy field fields, our model still outperforms `LACosmic` by $\geq 20\%$ in TPR. The advantages are more significant at very low false detection rates, e.g., 75% TPR compared to 34% for `LACosmic` in resolved galaxy fields, at a FPR of 0.05%. Figure 4.1 shows examples of mask prediction by `deepCR` and `LACosmic` in resolved galaxy fields. As seen in the figure, CR mask predicted by `deepCR` is mostly identical to ground truth in all cases, while `LACosmic` tends to miss larger cosmic rays and is prone to false detections. Further quantitative comparison is presented in Table 2, which also lists runtime required to predict one hundred 256×256 image

Table 3. Image inpainting metrics of deepCR-inpaint as compared to baseline models. MSE is average mean squared error of 48 test iterations, each iteration containing 200 image stamps and their respectively inpainting mask randomly sampled from the test set. The last two columns shows runtime to predict one hundred 256×256 image stamps, evaluated either on 4 cores of an Intel Xeon CPU, or one Nvidia Titan X GPU.

Model	extragalactic	globular cluster	resolved galaxy	runtime	
	MSE	MSE	MSE	CPU	GPU
deepCR-2-32	0.012	0.034	0.503	7.5s	0.2s
deepCR-3-32	0.012	0.033	0.479	12.7s	0.3s
medmask	0.105	1.511	5.946	1.0s^a	n/a
biharmonic	0.041	0.669	2.578	109.5s	n/a

^aEstimation from a single threaded implementation, which took 8.0 seconds on average.

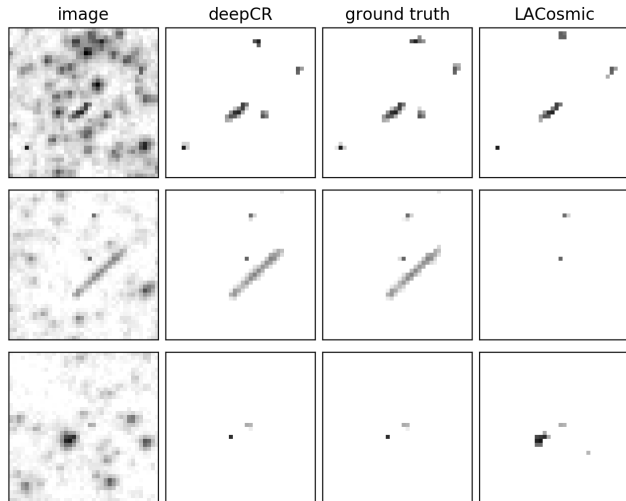


Figure 5. Comparison of deepCR-mask-2-32 and LACosmic in resolved galaxy fields. Columns from left to right are: input image, deepCR predicted CR, ground truth CR, and LACosmic predicted CR. Threshold for deepCR is set to 0.5 while LACosmic uses the following parameters: objlim=5, sigclip=10, where the threshold sigclip, is chosen to balance true detection and false detection. deepCR prediction is mostly identical to ground truth in all cases. Rows 1 and 2 shows the tendency of LACosmic to miss either the peripheral or the entirety of larger CRs. Rows 1 and 3 show cases where LACosmic misidentifies stars as cosmic rays.

stamps. We find that the smaller variant, deepCR-2-4, runs around 90 times faster than LACosmic on one Nvidia Titan X GPU, and 6 times faster on CPU. CPU implementation of each model is well parallelized and fully utilized 4 cores on an Intel Xeon CPU.

4.2. Replacing Masked Pixels: deepCR-inpaint

We evaluate deepCR-inpaint against non-neural baseline models including biharmonic interpolation (scikit-image) and masked median sampling (5×5 filter; medmask) that is used by LACosmic. Evaluation is done on 9600 images stamps randomly chosen from the test set, with different generated inpainting mask

applied to each one of them. The masks are generated as described in Section 3, with the number of added mask for each image stamp fixed at 1 to preserve the native mask density in the test set. By fixing numpy random seeds, we make sure all models are evaluated on the same sequence of image stamps with the same generated masks.

Inpainting performances and runtimes are listed in Table 4, which shows that deepCR achieves MSEs 20 times lower in globular cluster fields, 5 times lower in resolved galaxy fields, and 2.5 times lower in extragalactic fields, compared to the best performing non-neural method, biharmonic inpainting. Our model is also drastically faster than non-neural models on GPU. Between the non-neural models, biharmonic is more accurate than masked median sampling, though at a cost of $100 \times$ compute. Well-threaded implementation of median masked sampling remains the fastest method on CPU. Although deepCR-inpaint is comparably accurate, we caution that further testing with astronomically meaningful metrics (such as photometric fidelity) is required, before the inpainted pixels can be used for science.

4.3. Usage

To accompany this paper we provide a Python package called deepCR which can be installed via PIP. The models trained on HST ACS/WFC F606W data which are used in this paper are shipped along with the code. If IMAGE is a 2-dimensional numpy image array that contains cosmic rays, the procedure to predict a cosmic ray mask (MASK) and a clean image (CLEANED_IMAGE) is as follows:

```

from deepCR import deepCR
mdl = deepCR(mask="ACS-WFC-F606W-2-32",
              inpaint="ACS-WFC-F606W-3-32",
              device="GPU")
mask, cleaned_image = mdl.clean(image)

```

deepCR is first instantiated with the specified model configuration, before applying to data. Non-neural in-

painting could be used in place of deepCR-inpaint by setting `INPAINT="MEDMASK"`. We intend to host a “model zoo” for models learned on other instrumental configurations and welcome community engagement to generate such models and to improve the code.

5. SUMMARY

We have presented a novel deep learning based approach for cosmic ray rejection, and showed that after proper training, it has the potential to outperform current methods in terms of both speed and accuracy in mask prediction and image inpainting. At a false positive rate of 0.5%, `deepCR` achieves close to 100% detection rates in extragalactic and globular cluster fields, and 91% in resolved galaxy fields, which is a significant improvement over current state-of-the-art. Compared to a well-threaded implementation of `LACosmic`, `deepCR` mask predictions runs up to 650% faster on CPU and 90× faster on GPU. As for inpainting, mean squared error of deepCR-inpaint predictions are 20 times lower in globular cluster fields, 5 times lower in resolved galaxy fields, and 2.5 times lower in extragalactic fields, compared to the best performing non-neural technique. The superior MSE performance of the `deepCR`-inpaint over generic interpolation schemes is not surprising, given that our model is trained on the semantically constrained domain of astronomical images. To facilitate reproducibility of these results, we have released the benchmarking codebase.²

While `LACosmic` requires fine tuning of `objlim` for different instrumental setups to maximize CR detection accuracy and minimize false detection, our approach requires training on a set of cosmic ray labeled images that are representative of new data expected from the data reduction pipeline adapting `deepCR`. Since CNN models are based on pattern recognition learned from training data, new training data might be required if predictive data differs significantly from training data. Our work has focused on HST ACS/WFC imaging in a sin-

gle filter for which there was readily available training data across a variety of field types. However, we suggest models trained on one particular filter of a detector will likely perform well on other filters of the same detector, and more likely on filters of longer wavelengths, for with wider PSFs sources of confusion would have less resemblance to cosmic rays. Indeed, in our preliminary experiments, we blindly applied the `deepCR`-mask trained on the ACS/WFC F606W filter to ACS/WFC F814W data, and found comparable performance. As we have trained a single model to work across three different types of fields, it should also be possible to train a well-performing model on several different filters of the same detector, with similar amount of training data.

Looking ahead, we speculate that it may be feasible to train a single model not only on different filters, but also on different detectors and telescopes, though this would certainly require larger capacity models and more sophisticated data pre-processing. We have not experimented with spectroscopic data nor ground-based data, but expect our approach to work as well. To facilitate the use of the `deepCR` framework in real-world reduction pipelines, we have made our code with the ACS/WFC F606W trained models available as an open source project, and we encourage the community to contribute by training additional models that allows `deepCR` to be used in a wide range of detector configurations.

Software: `astropy` (Astropy Collaboration et al. 2013; Collaboration et al. 2018), `astrodrizzle` (Hack et al. 2012), `numpy` (van der Walt et al. 2011), `scipy` (Jones et al. 2001), `matplotlib` (Hunter 2007), `astroscrappy` (McCully et al. 2018), `pytorch` (Paszke et al. 2017a), `Jupyter` (Kluyver et al. 2016), `Scikit-image` (van der Walt et al. 2014)

It is a pleasure to acknowledge Stéfan van der Walt for helpful conversations and for comments on a draft of this manuscript. This work was supported by a Gordon and Betty Moore Foundation Data-Driven Discovery grant.

REFERENCES

- Astropy Collaboration, Robitaille, T. P., Tollerud, E. J., et al. 2013, *A&A*, 558, A33
- Astropy Collaboration, Price-Whelan, A. M., Sipőcz, B. M., et al. 2018, *The Astronomical Journal*, 156, 123. <https://doi.org/10.3847/1538-3881/aabc4f>
- Deng, J., Dong, W., Socher, R., et al. 2009, in *CVPR*
- Farage, C. L., & Pimblet, K. A. 2005, *Publications of the Astronomical Society of Australia*, 22, 249. <http://adsabs.harvard.edu/abs/2005PASA...22..249F>
- Florentin-Nielsen, R., Andersen, M. I., & Nielsen, S. P. 1995, in *New Developments in Array Technology and Applications*, ed. A. G. D. Philip, K. A. Janes, & A. R. Uppgren (Dordrecht: Springer Netherlands), 207–211

² <https://github.com/kmzzhang/deepCR-paper>

- Groom, D. 2004, in *Astrophysics and Space Science Library*, Vol. 300, *Scientific Detectors for Astronomy, The Beginning of a New Era*, ed. P. Amico, J. W. Beletic, & J. E. Beletic, 81–93
- Hack, W. J., Dencheva, N., Fruchter, A. S., et al. 2012, in *American Astronomical Society Meeting Abstracts*, Vol. 220, *American Astronomical Society Meeting Abstracts #220*, 135.15
- Hunter, J. D. 2007, *Computing in Science and Engineering*, 9, 90
- Jones, E., Oliphant, T., Peterson, P., et al. 2001, *SciPy: Open source scientific tools for Python*, <http://www.scipy.org/> accessed: 2019-07-20
- Kingma, D. P., & Ba, J. 2015, in *ICLR*, arXiv: 1412.6980. <http://arxiv.org/abs/1412.6980>
- Kluyver, T., Ragan-Kelley, B., Pérez, F., et al. 2016, in *Positioning and Power in Academic Publishing: Players, Agents and Agendas*, ed. F. Loizides & B. Schmidt, IOS Press, 87 – 90
- LeCun, Y., Bengio, Y., & Hinton, G. 2015, *Nature*, 521, 436. <https://www.nature.com/articles/nature14539>
- Lehtinen, J., Munkberg, J., Hasselgren, J., et al. 2018, in *ICML*. <http://proceedings.mlr.press/v80/lehtinen18a.html>
- McCully, C., Crawford, S., Kovacs, G., et al. 2018, *astropy/astrocrappy: v1.0.5 Zenodo Release*, doi:10.5281/zenodo.1482019. <https://doi.org/10.5281/zenodo.1482019>
- Murtagh, F. D., & Adorf, H. M. 1991, in *European Southern Observatory Conference and Workshop Proceedings*, Vol. 38, 51
- Paszke, A., Gross, S., Chintala, S., et al. 2017a, in *NIPS Autodiff Workshop*
- Paszke, A., Gross, S., Chintala, S., et al. 2017b, in *NIPS*
- Pych, W. 2004, *Publications of the Astronomical Society of the Pacific*, 116, 148. <http://adsabs.harvard.edu/abs/2004PASP..116..148P>
- Rhoads, J. E. 2000, *Publications of the Astronomical Society of the Pacific*, 112, 703. <http://adsabs.harvard.edu/abs/2000PASP..112..703R>
- Ronneberger, O., Fischer, P., & Brox, T. 2015, in *MICCAI*, arXiv: 1505.04597. <http://arxiv.org/abs/1505.04597>
- Salzberg, S., Chandar, R., Ford, H., Murthy, S. K., & White, R. 1995, *Publ. Astro. Soc. Pac.*, 107, 279
- Shelhamer, E., Long, J., & Darrell, T. 2017, *IEEE Transactions on Pattern Analysis and Machine Intelligence*, 39, 640
- van der Walt, S., Colbert, S. C., & Varoquaux, G. 2011, *Computing in Science Engineering*, 13, 22
- van der Walt, S., Schönberger, J. L., Nunez-Iglesias, J., et al. 2014, *PeerJ*, 2, e453. <https://peerj.com/articles/453>
- van Dokkum, P. G. 2001, *Publications of the Astronomical Society of the Pacific*, 113, 1420. <http://adsabs.harvard.edu/abs/2001PASP..113.1420V>
- Windhorst, R. A., Franklin, B. E., & Neuschaefer, L. W. 1994, *Publ. Astro. Soc. Pac.*, 106, 798

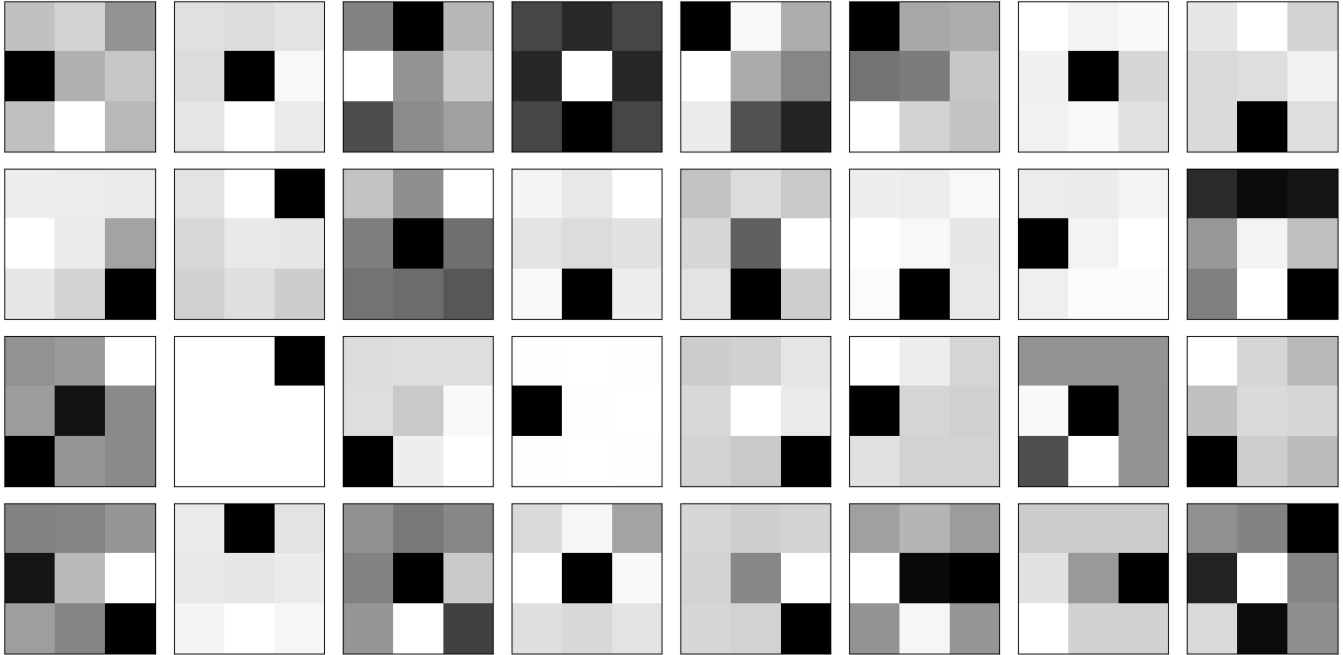


Figure 6. Example convolution kernels in the first layer of from a learned `deepCR-mask` model. Gray-scale level is relative within each subplot. The networks learn a diversity of filters, including one that resembles the Laplacian kernel used in `LACosmic` (4th kernel from the left on the 1st row.) Note: not all models produce Laplacian looking kernels.

APPENDIX

A. TRAINING PROCEDURES

We implemented `deepCR` models in `PYTORCH 1.0` (Paszke et al. 2017b). We follow the steps described below to train both `deepCR-mask` and `deepCR-inpaint`. The network is first trained for 20 epochs in “training mode” for which batch normalization layers keep a running statistics of layer activations with momentum of 0.005, and use training batch statistics for normalization. Following the initial 20 epochs of training (40 for `deepCR-inpaint`), the network is set to “evaluation mode” where the running statistics are frozen and used in both forward and backward passes of batch normalization. This procedure ensures that batch normalization statistics used at training and test time are identical, which helps the network achieve lower loss at test time. Given the large dynamic range of astronomical imaging data, we have found this technique to be essential.

We set the initial learning rate to 0.005 and 0.01 for `deepCR-mask` and `deepCR-inpaint` respectively, and use the `ADAM` optimizer (Kingma & Ba 2015). Learning rate decays by a factor of 0.1 automatically whenever validation loss does not improve by 0.1% for 4 epochs. We stop training once validation loss does not improve after two rounds of learning rate decay. Both `deepCR-mask` variants converged within 60 epochs of training, while `deepCR-inpaint` variants took a longer 220-epoch training. Each epoch of training took less than 1 minute on 4 Nvidia Tesla GPUs. Figure A shows a visualization of filters of the `deepCR-mask` in the first convolution layer.